SPECIAL ISSUE ARTICLE

PROGRESS IN
PHOTOVOLTAICS WILEY

Versatile implied open-circuit voltage imaging method and its application in monolithic tandem solar cells

Oliver Fischer[1,2] 🄙 | Anh Dinh Bui[3] 🄙 | Florian Schindler[1] 🄙 | Daniel Macdonald[3] | Stefan W. Glunz[1,2] 🄙 | Hieu T. Nguyen[3] | Martin C. Schubert[1]

[1]Fraunhofer Institute for Solar Energy Systems ISE, Freiburg, Germany

[2]Chair for Photovoltaic Energy Conversion, Department of Sustainable Systems Engineering INATECH, University of Freiburg, Freiburg, Germany

[3]School of Engineering, The Australian National University, Canberra, Australian Capital Territory, Australia

Correspondence
Oliver Fischer and Martin C. Schubert, Fraunhofer Institute for Solar Energy Systems ISE, Heidenhofstr. 2, 79110 Freiburg, Germany.
Email: oliver.fischer@ise.fraunhofer.de and martin.schubert@ise.fraunhofer.de

Anh Dinh Bui and Hieu T. Nguyen, School of Engineering, The Australian National University, Canberra, Australian Capital Territory, Australia.
Email: anh.bui@anu.edu.au and hieu.nguyen@anu.edu.au

Funding information
Australian Renewable Energy Agency, Grant/Award Number: 2022/TRAC001; German Federal Ministry for Economic Affairs and Climate Action (BMWK), Grant/Award Numbers: 03EE1087B, 03EE1087A; European Union's Horizon 2020, Grant/Award Number: 101006715

Abstract

As the efficiency of perovskite silicon tandem solar cells is increasing, the upscaling for industrial production is coming into focus. Spatially resolved, quantitative, fast, and reliable contactless measurement techniques are demanded for quality assurance and to pinpoint the cause of performance losses in perovskite silicon tandem solar cells. In this publication, we present a measurement method based on spectrally integrated photoluminescence (PL) imaging to extract subcell-selective implied open-circuit (iV_{oc}) images from monolithic perovskite silicon tandem solar cells. We validate the approach using spectrally resolved absolute PL measurements based on an integrating sphere for the perovskite top cell and PL-calibrated carrier lifetime images for the silicon bottom cell. Additionally, V_{oc} measurements of solar cells with low contact losses are used to validate the new measurement technique. We find a good agreement of the iV_{oc} images with the validating measurements with a maximum deviation of well below 1% compared to the validation measurements.

KEYWORDS

imaging, iV_{oc}, loss analysis, perovskite silicon tandem solar cell, photoluminescence

1 | INTRODUCTION

Recent remarkable progress in research and development of monolithic perovskite silicon tandem solar cells lead to certified power conversion efficiencies (PCE) of up to 33.7%.[1] However, further optimization of this technology is necessary for its successful commercialization. First, in comparison to the theoretical limit of exceeding 40%,[2–4] there exists

a significant gap in improving device structures, materials, and passivation technology to fully realize the potential of tandem solar cells. Second, it is worth noting that most of the reported high-performance devices have been achieved with small areas of approximately 1 cm^2.[1,5] However, when scaling up to large area devices, the challenge lies in achieving homogeneous deposition of the multiple layers, particularly the perovskite absorber, since inhomogeneities often result in performance-degrading defects.[6,7] Moreover, even at the nanoscale, the presence of local impurities in the perovskite top cells can serve as

---

Oliver Fischer and Anh Dinh Bui contributed equally to this work.

degradation centers, negatively impacting the long-term operation of the device.[8] Addressing these challenges is vital to enable large-scale mass production and necessitates the early-stage evaluation of solar cell quality during the optimization processes. A profound understanding of the photovoltaic parameters and the underlying causes of losses is imperative to successfully accomplish this objective.[9]

The open-circuit voltage V_{oc} is a crucial parameter for assessing the quality of perovskite silicon tandem solar cells. From this value, other optoelectronic parameters such as pseudo fill factor, ideality factor, and activation energy of recombination can be estimated.[10,11] These parameters, in turn, allow for the estimation of performance losses resulting from non-radiative recombination and series resistance in a device.[12,13] However, since V_{oc} is just a global value, it fails to provide insights into the influence of local defects on the overall device performance. Additionally, V_{oc} can only be measured in the final assembled device, limiting its usefulness in early-stage material selection. Moreover, V_{oc} is affected not only by local or homogeneously distributed defects and recombination sites in the bulk and at interfaces but also by energy barriers at various material interfaces within the solar cell stack.[14] Therefore, to gain a more comprehensive understanding of the limitations of large-area perovskite silicon tandem solar cells, a thorough evaluation of the influence of local defects and interface energy barriers is insightful. In this context, the implied open-circuit voltage iV_{oc}, related to the quasi-Fermi level splitting (QFLS), offers a valuable alternative. iV_{oc} represents the maximum theoretically achievable V_{oc} (i.e., the V_{oc} of a solar cell with no contact losses) and can be measured in contactless mode. Therefore, it holds potential for the application in early-stage material selection processes.[15] In addition, it plays a crucial role in distinguishing between internal losses in the active layer caused by defects and losses resulting from energy barriers.[16,17] Last but not least, since iV_{oc} can be separately measured for each subcell, it serves as a useful parameter for understanding and diagnosing subcell performance in multi-junction photovoltaic devices.[18,19]

Several measurement techniques can be applied to determine the iV_{oc} of photovoltaic devices. While spectrally resolved absolute average photoluminescence (PL) measurements have been commonly used to extract the spatially averaged iV_{oc},[20,21] they lack spatial information and are unsuitable for large solar cells with local defects as they cannot pinpoint the exact location of the defects. An alternative approach is micro-PL mapping, which allows obtaining iV_{oc} maps,[22,23] but it suffers from long measurement durations for large samples, limiting the high sample throughput. A promising solution is provided by the hyperspectral imaging method, which allows the acquisition of spatially resolved iV_{oc} images within reasonable measurement durations.[24,25] However, this method requires complex and tunable filters. Another simpler and faster method is a PL-calibrated carrier lifetime measurement,[26–28] widely used in silicon solar cells, but it is not suitable for the top cell of tandem devices due to the lack of information on doping densities and dopant types, as well as the relatively short carrier lifetime that is challenging to measure. Fortunately, spectrally integrated absolute calibrated PL imaging methods[29,30] can overcome these challenges by offering a cheap, fast, and spatially resolved

approach to selectively capture the iV_{oc} image of each subcell in a tandem device.

In this work, we present a method that enables fast iV_{oc} imaging on various devices including single junction and tandem solar cells. First, we describe the procedure to convert the relative PL signal to iV_{oc}. Unlike Soufiani et al.,[29] we utilize wide range bandpass filters, allowing the flexible application of the method to perovskite solar cells with various band gaps. Additionally, the use of wide range bandpass filters improves the signal-to-noise ratio and enables capturing the signal at low excitation intensity, which is useful for further characterization methods, such as the Suns-PL method.[31–33]

To calculate iV_{oc} from the detected PL signal, precise knowledge of the absorptance A is essential. In previous studies, absorptance was extracted from measured reflectance and transmittance spectra.[29,30] However, the direct determination of absorptance from reflectance and transmissivity is not possible for tandem devices or fully completed solar cells with back electrodes. Therefore, this work accesses the absorptance precisely also in tandem devices or fully completed solar cells with the use of simulated absorptance spectra or external quantum efficiencies (EQEs). The use of EQEs to approximate A was also applied in the past for hyperspectral imaging.[25] In contrast to the approach in Soufiani et al.,[29] this allows to include a larger part of the PL spectrum and not only restricts the spectral range to the high energy tail of the PL signal with constant absorptance. This helps to overcome the limitation of low measurement signal in the high-energy tail of the PL spectrum. Moreover, Soufiani et al.[29] investigated thick perovskite layers and single junction solar cells, where the absorptance in the high energy tail of the PL peak can be assumed to be constant. However, the absorptance is not constant in the high energy tail if the absorber is not sufficiently thick. While a thinner perovskite absorber layer is not desirable in a perovskite single junction solar cell, this can be a desired device design in perovskite silicon tandem solar cells, as presented in, for example, Heydarian et al.,[21] for reasons of current matching.

Moreover, instead of relying on the terminal V_{oc},[30] which is challenging to measure for each subcell in tandem devices, we employ a reference light source with known power spectrum following the approach in Soufiani et al.[29] This approach enables us to overcome the difficulty of directly measuring the terminal voltage of each subcell in monolithic tandem devices. Our method is validated with different independent measurements including PL-calibrated carrier lifetime, spectrally resolved absolute PL, and terminal V_{oc} measurements. Finally, the method is utilized to evaluate the performance and investigate local losses of each subcell in a tandem solar cell.

2 | METHODS

2.1 | PL imaging setup

The commercial measurement system "Tandem Modulum," developed at Fraunhofer ISE and built by Intego GmbH, was used for the acquisition of PL images. The system is schematically displayed in Figure 1. The perovskite silicon tandem solar cell can be excited subcell-
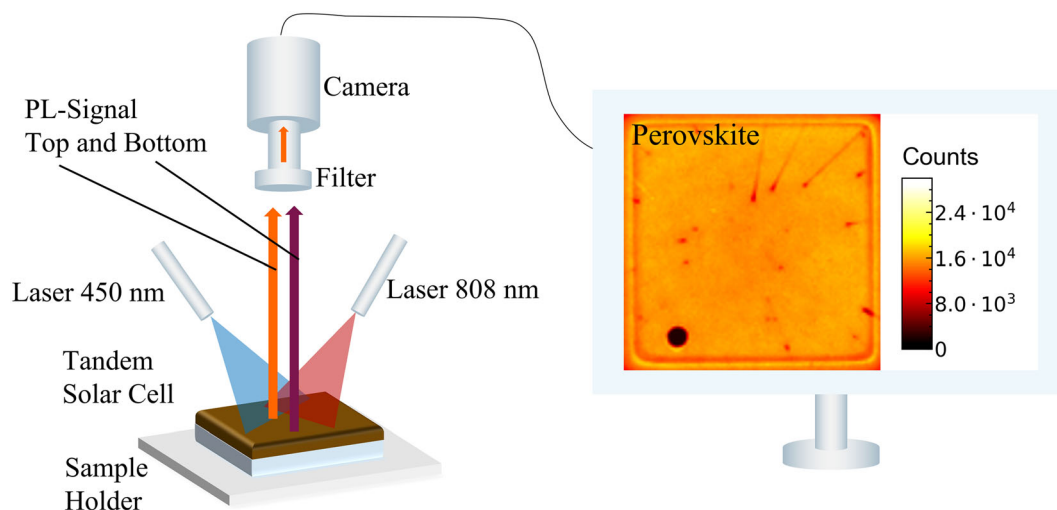
FIGURE 1 Spectrally integrated PL imaging setup. PL images of a tandem solar cell that is placed on a temperature controllable sample holder can be acquired with the help of two lasers and bandgap filters.
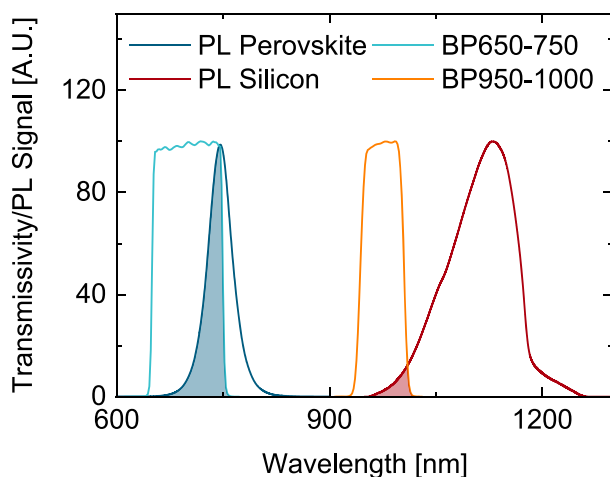
FIGURE 2 Exemplary bandpass filter spectra used for the spectrally integrated PL measurements and PL spectra of each subcell in perovskite silicon tandem solar cells measured with a hyperspectral measurement system. The part of the PL spectrum detected in the spectrally integrated PL imaging setup is shaded.

selectively using a 450 nm laser for the perovskite top solar cell and an 808 nm laser for the silicon bottom solar cell. The PL images are acquired using a silicon CCD camera. The quantum efficiency (QE) of the camera provided by the manufacturer is displayed in Figure S1. Appropriate optical bandpass filters are used to block the laser radiation and separate the luminescent signal from both subcells. For illustration, exemplary PL spectra and corresponding bandpass filter spectra are shown in Figure 2. The shaded part of the PL spectrum marks the part of the spectrum that is detected in the camera. In contrast to hyperspectral PL images, PL images that are acquired with a camera and a non-tunable bandpass filter contain no detailed information on the spectrum of the PL signal. These PL images simply show the total PL signal from the sample in the spectral range where the

bandpass filter transmits light. We therefore refer to this PL imaging method as spectrally integrated PL imaging. The samples were illuminated before the image acquisition to reach stabilized conditions for measurements on perovskite subcells. For the measurements in open-circuit mode, the perovskite and silicon subcells are individually illuminated at 1-sun equivalent conditions. This means that each subcell is illuminated with the photon flux that it would encounter in the tandem device under the AM1.5G spectrum. The 1-sun equivalent photon currents are calculated using the EQEs or absorptance curves of the subcells following the approach from Meusel et al.[34] For this, the spectra of the two lasers are assumed to be Gaussian shaped with peak widths according to the manufacturer's data sheets. The temperature of the sample holder can be controlled and measured to prevent temperature effects in the measurements.

2.2 | Extraction of iV_{oc} images

In this section, we describe the method to extract iV_{oc} images from PL images. The individual steps are displayed in a graphical algorithm in Figure S2. In a first step, the energy-dependent spectral response $SR(E)$ of the system is determined. $SR(E)$ accounts for the energy dependent transmission of photons through the optic components in the light path and the capture probability in the camera. It is the product of the transmission spectrum of the optical filters, the transmission spectrum of the objective and the QE of the camera. While the spectra of the optical filters and the objective are measured inhouse using a Lambda 950 spectrometer with a 150 mm integrating sphere from PerkinElmer, the QE in Figure S1 is provided by the camera manufacturer. In the next step, the scaling factor SF is determined. SF considers that only a small fraction of the total emitted PL photon flux is emitted in the direction of the camera and can be collected.[35] A calibration lamp (ISS-5P-SR-FS from Gigahertz-Optik) with a known

spectrum and spatially uniform photon flux $j_{ph,lamp}$ is used to determine SF according to Equation (1).

$$\sum_{x=1}^{n} I_{x,lamp}/n = SF \int_0^{\infty} SR(E) \, j_{ph,lamp}(E) \, dE \quad (1)$$

In Equation (1), $I_{x,lamp}$ is the number of counts in the pixel at position x on the image of the calibration lamp with a total of n pixels. Note that due to the calibration procedure of SF, only the shape of all spectra, including the QE of the camera and the transmissivity of the filters, must be known. Any deviation by a constant factor of the measured spectra from the true spectra will be accounted for in the calibration of SF.

In the last step, the generalized Planck's law[36,37] is used. Equation (2) shows the relationship of the locally detected PL signal intensity $I_{x,PL}$ at pixel x to $iV_{oc,x}$ that is present at pixel x.

$$I_{x,PL} = SF \exp\left(\frac{q \, iV_{oc,x}}{k_b T}\right) \frac{8\pi}{c^3 h^3} \int_0^{\infty} SR(E) \, A(E) \, E^2 \exp\left(-\frac{E}{k_b T}\right) dE \quad (2)$$

In Equation (2), q is the elementary charge, k_b is the Boltzmann constant, T is the absolute temperature measured on the sample, c is the speed of light, h is the Planck constant, and $A(E)$ is the energy-dependent absorptance of the photoactive layer. With this relation, the PL images can then be converted to iV_{oc} images. Note that for reasons of readability, we will write iV_{oc} instead of $iV_{oc,x}$ when referring to a local position in the following.[35]

## 2.3 | Determination of $A(E)$

$A(E)$ is an important parameter for iV_{oc} determination but it cannot be determined easily for certain substrate structures. In the following, we describe three approaches used in this publication to determine $A(E)$, depending on the solar cell architecture and available data.

For bifacial single junction devices or single absorptance layers that are deposited on glass, $A(E)$ can easily be extracted with a spectrometer using $A(E) = 1 - R(E) - T(E)$, with the reflectance $R(E)$ and the transmittance $T(E)$. We use a Lambda 950 spectrometer with a 150 mm integrating sphere from PerkinElmer for the measurements in our work. However, directly measuring $A(E)$ is challenging for both completed single junction solar cells with full area back contact metallization and individual subcells in monolithic tandem configuration. To circumvent this challenge, we suggest two alternative methods on how to acquire $A(E)$.

One alternative approach to obtain $A(E)$ is through simulations using raytracing in the silicon bottom cell and the transfer-matrix method for the perovskite top cell. The simulation methodology is described in detail in a previous work.[38] However, setting up an accurate simulation for $A(E)$ can be a challenging task since multiple input parameters of the simulation are required.

Therefore, another alternative and simpler method approximates $A(E)$ based on the measurable EQE $EQE(E)$. Studies comparing the photo- and electro-luminescence spectra curves of silicon and
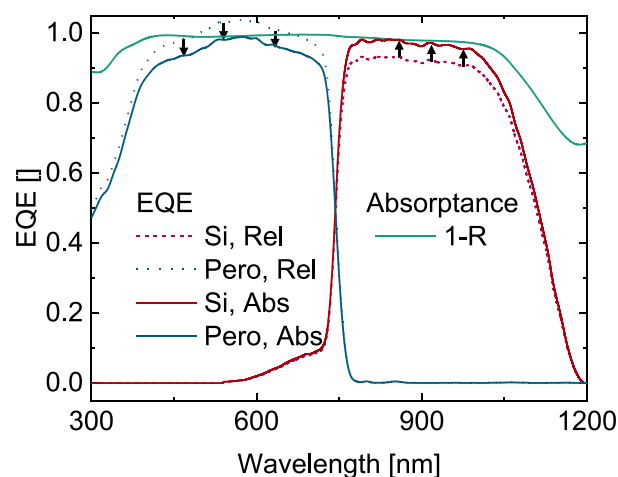

FIGURE 3 Visualization of scaling procedure of EQEs.

perovskite solar cells suggest that $A(E)$ and $EQE(E)$ spectra are very similar.[25,39,40] Simulation data also suggest that the absorptance can be approximated by $EQE(E)$.[21] However, measuring *absolute* EQEs $EQE_{abs}(E)$ is challenging for multijunction solar cells, especially for metastable monolithic perovskite silicon tandem solar cells.[41–44] A scaling factor SF_{EQE} needs to be determined to extract $EQE_{abs}(E)$ from the as-measured EQE $EQE_{rel}(E)$, using $EQE_{abs}(E) = SF_{EQE} \, EQE_{rel}(E)$. SF_{EQE} is energy-independent and can be determined from spectrometric measurements.[34] However, since spectrometric measurements are time-consuming, we suggest using faster spectrometer-based measurements of $R(E)$ to approximate $EQE_{abs}(E)$. We assume that parasitic absorptance $A_{para}(E)$ can be neglected at least for one particular energy E_0 in the spectrum and that $T(E_0) = 0$. Then, $A(E_0) + R(E_0) = 1$ holds true at this point. Assuming further that $A(E_0) = EQE_{abs}(E_0)$, we can determine SF_{EQE} and scale $EQE_{rel}(E)$ to $EQE_{abs}(E)$ as depicted in Figure 3. Note that this procedure does not imply that $EQE_{abs}(E) + R(E) = 1$ for all E. For example, in the low energy part $T(E) \neq 0$ and in other regions, $A_{para}(E)$ might not be neglectable. The errors introduced by this scaling procedure are small, as discussed in Section 3.

3 | RESULTS AND DISCUSSION

3.1 | Method validation

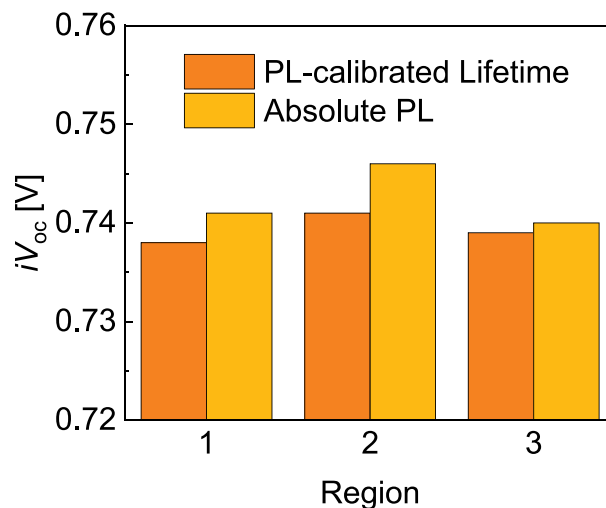#### 3.1.1 | Comparison with PL-calibrated carrier lifetime measurements

First, we validate our calibration procedure and calculation on a planar p-type silicon wafer with an amorphous silicon passivation layer by comparing an iV_{oc} image extracted from an absolute PL image versus iV_{oc} images from carrier lifetime measurements[27] (see the chapter "Carrier Lifetime Imaging" in the Supporting Information for details on the carrier lifetime measurements). A bandpass filter covering the spectral range from 950 nm to 1000 nm (denoted as BP950-1000)
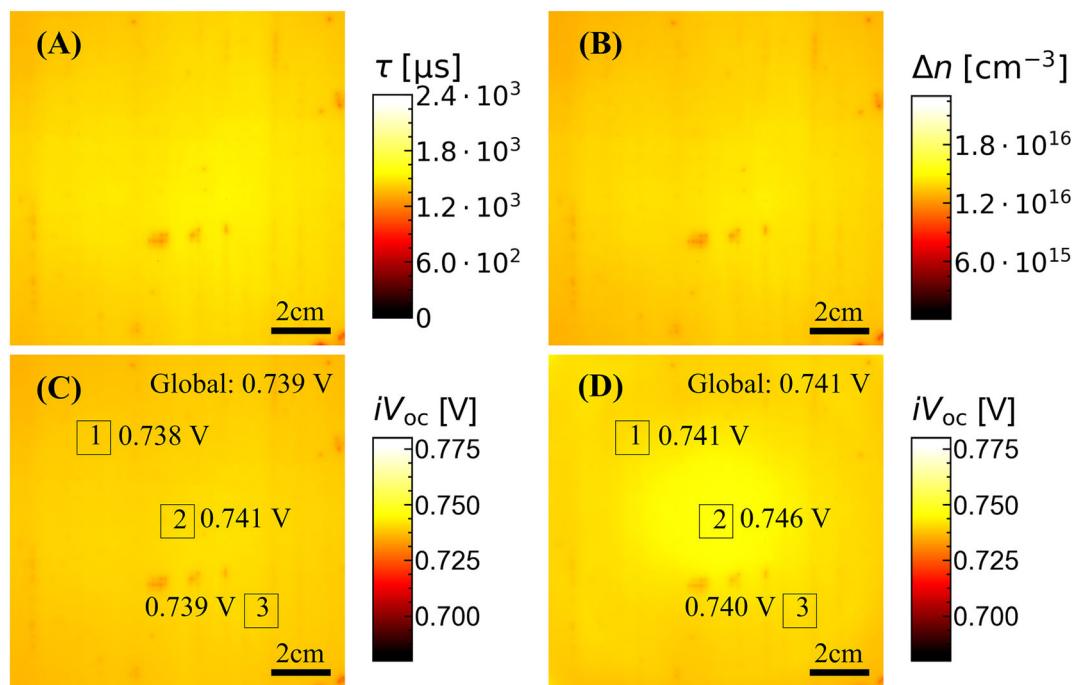
FIGURE 4 Based on PL-calibrated carrier lifetime images (A) and excess carrier concentration distribution (B) an iV_{oc} image can be calculated (C). In comparison, the iV_{oc} image based on absolute PL measurements according to our method is displayed in (D). The three rectangular regions marked in (C) and (D) are used for a comparison in Figure 5. The substrate presented is a p-type FZ silicon wafer with amorphous silicon passivation. The bright spot in (D) is due to reflections that are more pronounced with the optical components used in (D) compared to (C).

was used to detect the high energy tail of the PL signal for the PL image. Reflectance and transmittance spectra were used to approximate the absorptance curve of the p-type silicon wafer shown in Figure S4. Figure 4A,B illustrates the carrier lifetime image and excess carrier concentration (Δn) image obtained from carrier lifetime measurement. Figure 4C shows the iV_{oc} image calculated from the Δn image. Figure 4D displays the iV_{oc} image of the silicon wafer, which was extracted using our proposed method. Since the measurements for Figure 4C,D were conducted on different setups with different measurement geometries, the bright, centered spot (caused by a reflection of the measurement signal) is more pronounced in Figure 4D than in Figure 4C. Whereas the first setup has been optimized with respect to measurements on planar samples, that is, imaging artifacts due to parasitic luminescence or reflections have been reduced to a minimum, this optimization has not been performed yet for the second setup. Thus, the bright spot in the center of Figure 4D can be attributed to a reflection artefact and is not an inherent error of the iV_{oc} imaging method presented here.

Figure 5 shows the observed small variations between Figure 4C and Figure 4D. For instance, the average values of region 1 in Figure 4C,D are 0.738 V and 0.741 V, respectively, resulting in a relative deviation of less than 0.4%. In region 2, a reflected signal leads to an increase in iV_{oc} in Figure 4D. Still, iV_{oc} based on absolute PL-measurements is less than 0.7% higher compared to iV_{oc} extracted from PL-calibrated carrier lifetime measurements in Figure 4C. We conclude that a very good agreement between both measurements is

FIGURE 5 Comparison of mean iV_{oc} in regions 1, 2, and 3 in Figure 4 determined with the use of PL calibrated carrier lifetime measurements and absolute PL measurements. The data are also presented in Table S2.

achieved. As Figure S3 shows, similar results are also found for n-type multicrystalline silicon wafers. It is worth noting that while the PL-calibrated carrier lifetime method is restricted to silicon materials, our proposed method is applicable to a wide range of materials, making it highly versatile and valuable.

3.1.2 | Comparison with V_{oc} of full solar cell

In devices with high-quality transport layers and appropriate work functions, the deviation between the iV_{oc} versus terminal V_{oc} is negligible. Hence, $iV_{oc} \approx V_{oc}$ can be expected. The reliable quality of a silicon based standard World PV Scale (WPVS) reference cell and a III-V material based tandem solar cell allows us to use their external V_{oc} to validate our method. We use the iV_{oc} images of a p-type silicon WPVS cell to validate our measurements for the spectral range of silicon with a WPVS cell. Afterwards, a tandem device can be used to validate the spectral range of perovskite filters as well. A III-V tandem solar cell composed of $Ga_{0.35}In_{0.65}P/Ga_{0.83}In_{0.17}As$ with the bandgaps of 1.68 eV (738 nm) and 1.18 eV (1051 nm) for top cell and bottom cell,[45] respectively, serves for this purpose. The EQEs (compare Figures S5 and S6) do not need to be rescaled using the method described above. For the silicon single junction solar cell the EQE can be scaled to the short-circuit current. For the III-V tandem solar cell, a spectral metric measurement was available that allowed the precise scaling of the subcell EQEs.

Figure 6A displays the iV_{oc} image of a WPVS cell under 1-sun equivalent illumination. A BP950-1000 was used to detect the high energy tail of the PL signal. The mean value (calculated by averaging the iV_{oc} image excluding the fingers) of 0.644 V shows no measurable difference to the external V_{oc} measured at the electrode, which is also 0.644 V.

Figure 6B,C shows the iV_{oc} distributions of the top and bottom solar cell of the III-V tandem solar cell. A bandpass filter covering the spectral range from 650 nm to 750 nm (denoted as BP650-750) was used to detect the PL signal of the top solar cell. A BP950-1000 was used to detect the high energy tail of the PL signal of the bottom solar cell. The top solar cell in Figure 6B shows an average iV_{oc} of 1.202 V over the whole active area. The bottom solar cell in Figure 6C shows an average iV_{oc} of 0.739 V over the whole active area. This adds up to a total iV_{oc} of 1.941 V. Under the illumination of the subcells with both lasers, an average V_{oc} of 1.925 V can be measured at the terminals over a measurement duration of 10 s with an initial voltage of 1.926 V (laser intensity drops slightly over time). So iV_{oc} and V_{oc} deviate by approx. 16 mV. Possibly, this deviation is due to the local shunts or recombination sites in the top cell in Figure 6B. The

shunts lead to a local decrease of ≈ 40 mV in the iV_{oc} image. Hence, V_{oc} is also not expected to be uniform across the contact layer of the solar cell. The exact V_{oc} measured at the terminals depends on the unknown distribution of the V_{oc} in the contact layer. This cannot be reflected by any averaging method (here, we apply arithmetic averaging for the iV_{oc} images). However, regardless of the reason for this deviation, 16 mV correspond only to a relative increase of 0.8% of iV_{oc} compared to V_{oc}. It is therefore concluded that the agreement of iV_{oc} and V_{oc} is very good and that the iV_{oc} measurements are validated by the V_{oc} measurements.

3.1.3 | Comparison with absolute spectrally resolved PL measurements

In this section, we conduct PL measurements on two perovskite layers. The two layers are deposited on indium-tin-oxide-coated glass and are composed of $Cs_{0.05}FA_{0.85}MA_{0.1}PbI_{2.9}Br_{0.1}$ (with an additive) and $Cs_{0.05}(FA_{0.90}MA_{0.10})_{0.95}Pb(I_{0.95}Br_{0.05})_3$, respectively. This results in bandgaps of approximately 1.55 eV and 1.56 eV (800 nm and 795 nm), respectively. The absorptance spectra (see Figure S7) were extracted from reflectance and transmittance measurements. Due to parasitic absorptance of other layers in the device stack, it is important to only use the part around the PL spectrum peak where the parasitic absorptance is negligible compared to the absorptance of the perovskite layer. Hence, a bandpass filter covering the spectral range from 803 nm to 813 nm (denoted as BP803–813) was used to detect the PL signal of the samples. In the following, the iV_{oc} values obtained from our iV_{oc} imaging method are compared with data obtained from spectrally resolved absolute PL measurements using the LuQY Pro tool from QYB Quantum Yield Berlin (see "Absolute Spectrally Resolved PL Measurements" in the Supporting Information for details on the measurement setup).

Figure 7A,B presents the iV_{oc} images of the layers L1 and L2, respectively. Figure 7C shows the absolute PL spectra of the L1 and L2 samples acquired from the LuQY Pro tool. The iV_{oc} values were extracted by fitting the high-energy tail of the spectra. Figure 7D compares the iV_{oc} values extracted from the selected rectangular regions in Figure 7A,B, which correspond approximately to the
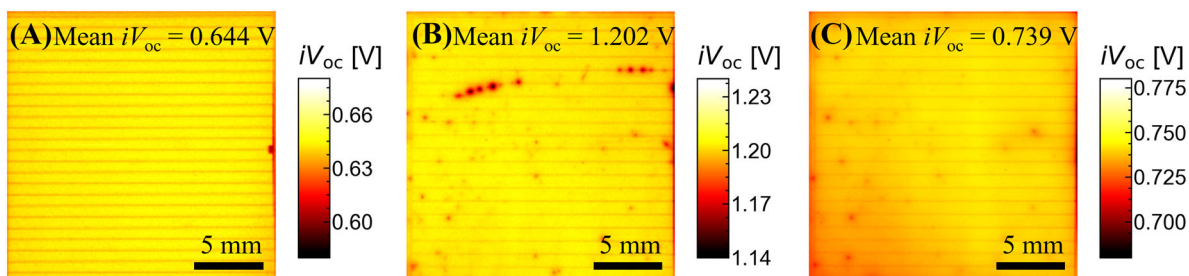
FIGURE 6 iV_{oc} images of a WPVS silicon solar cell (A) and the top (B) and bottom (C) cell of a III-V tandem solar cell illuminated under 1-sun equivalent conditions. V_{oc} of the WPVS solar cell is 0.644 V and hence equal to the determined iV_{oc}. The V_{oc} of the III-V tandem solar cell is 1.925 V, which is 16 mV below the sum of the determined subcell iV_{oc} values from (B) and (C) of 1.941 V.
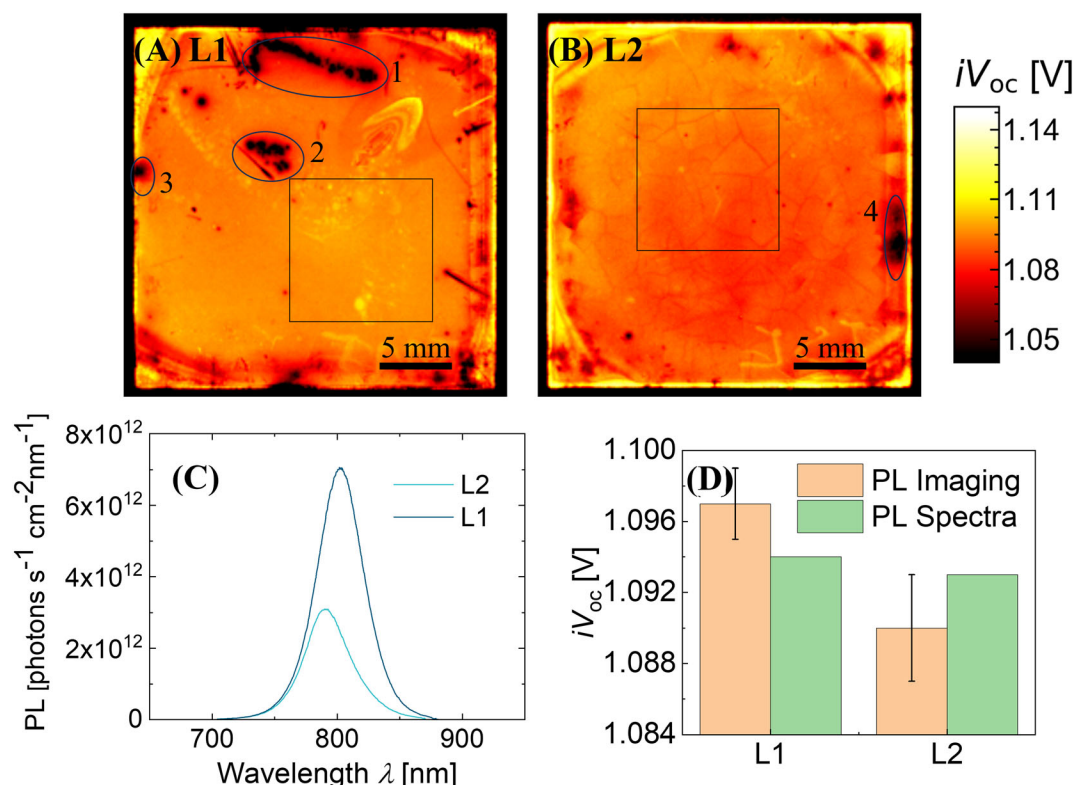
FIGURE 7 (A and B) iV$_{oc}$ images of two perovskite layers L1 and L2, respectively. The black squares mark the homogeneous regions used to calculate a mean iV$_{oc}$. (C) The absolute PL spectra of the devices measured with the LuQY Pro tool and (D) comparison of the mean iV$_{oc}$ in the selected regions in (A) and (B) versus the data extracted from (C). The error bars mark the standard deviation of the pixels considered for the mean value. The data of (D) can also be found in Table S3.

regions where LuQY measurements were performed using a single laser spot with an average size of 1 cm^2. For both devices, the deviation between the iV$_{oc}$ values obtained from our iV$_{oc}$ imaging method and the commercial tool is negligible, within 3 mV (compare Table S3). This small difference can be attributed to the metastable behavior of the perovskite material and instrument errors.

While our method provides similar results to the commercialized tool, it offers the advantage of spatially resolved information. For instance, as shown in Figure 7A,B, there are numerous low iV$_{oc}$ regions, some of which extend up to the millimeter scale, particularly around the edges of the devices (region 1, 3, and 4). Notably, even in the central area of L1, region 2 exhibits a significantly lower iV$_{oc}$ value ($\approx$50 mV lower than the average). These regions of low iV$_{oc}$ could be attributed to defects caused by non-optimized colloidal precursor solutions, process cleanliness, or nonradiative recombination in the bulk or at the interface of the perovskite layer. Such defects can significantly reduce the terminal voltage of the complete device.[46] Furthermore, over the long term, these defects can act as centers of degradation, leading to a rapid decline in device performance.[8] Overall, our findings highlight the effectiveness of our method in capturing spatial variations in iV$_{oc}$ and identifying potential defects in the perovskite layer that can impact device performance and stability.

3.1.4 | Uncertainty estimation

In this section, we carefully examine several measurement variables to develop a more thorough understanding of the potential causes of uncertainty of the data and how they can affect the accuracy of our data. This involves looking at measurement-related experiment errors and evaluating calculation errors that are introduced during the data processing stage. We thoroughly investigate these factors to quantify their impact and assess their importance in terms of the overall accuracy of our findings. We find that all investigated parameters influencing the measurement uncertainty result in errors well below 10 mV. For a perovskite solar cell with iV$_{oc} \approx$ 1200 mV, this leads to a measurement error of less than 1%.

Effect of the bandpass filter
To accurately measure the tandem device, it is necessary to employ different bandpass filters for each subcell to ensure proper collection of the PL signal from each subcell. Ideally, with an identical camera and objective and a precisely known spectrum of the calibration lamp, SF in Equation (1) should remain independent of the bandpass filter used. However, certain measurement errors, for example, errors in the shape of the spectrum of one of the measurement setup components, can occur. If these measurement errors differ for different spectral

ranges, their impact leads to variations in SF as well as potentially in the calculated iV_{oc}.

To evaluate the impact of these errors, we employed various bandpass filter configurations and calculated SF and iV_{oc} for the top cell of the III-V tandem solar cell used for comparison of iV_{oc} to V_{oc} in Figure 6. The resulting SF and iV_{oc} are displayed in Figure 8. We use the notation BP650-750 to denote a bandpass filter that transmits light in the spectral range from 650 nm to 750 nm. The configurations used were BP650-700, BP650-725, BP650-750, BP650-775, BP700-725, BP787-813, BP803-813, and BP950-1000. Figure 8A illustrates SF of our setup in dependence of the applied bandpass filter. For all configurations that allow capturing signals below 800 nm, the relative difference of the largest scaling factor compared to the smallest is found to be less than 14%. However, from Figure 8A, it seems that SF linearly decreases with the wavelength. Hence, for the bandgap BP950-1000 configuration, the calculated scaling factor for BP950-1000 is approximately 38% lower compared to the data in the BP650-750. The effect of these deviations on iV_{oc} depends on their root-cause. Since SF strictly decreases with increasing wavelength, the observed deviation is most likely attributed to an error in the spectrum rather than measurement noise. In the following we distinguish between two cases. In case 1, SF deviates due to an erroneous calibration lamp spectrum shape (so the real SF for all spectra optical components of the setup would be constant). In case 2, SF deviates due to an erroneous spectrum of the optical components (e.g., transmission filters or QE of the camera).

For case 1, the deviations in SF lead to an erroneous calibration of the setup and translate into an error in iV_{oc} because the erroneous spectrum affects only the calibration procedure. For the range from 650 nm to 850 nm the deviation in SF then corresponds to an approximate 4 mV fluctuation in the calculation of the iV_{oc} according to Equation (2). This would be consistent with the iV_{oc} data calculated from the top cell of the III-V tandem device, as shown in Figure 8B, where the difference between the highest and lowest iV_{oc} values is

approximately 6 mV. The deviation in SF for the BP950-1000 compared to the 650–850 nm region would result in an approximately 11 mV error in the iV_{oc} calculation. Note that a decreasing SF leads to an increase in iV_{oc} according to Equation (2). In consequence, the iV_{oc} of the silicon cell would be overestimated. This is unlikely, because for the silicon single junction cell presented in Figure 6A, we would then find $iV_{oc} < V_{oc}$. Alternatively, the iV_{oc} for the perovskite subcells in the short wavelength range is underestimated. This would suggest a larger deviation of iV_{oc} and V_{oc} in Figure 6B,C, which is physically possible but unlikely for a III-V material based tandem solar cell. Moreover, case 1 is unlikely, because the shape of the calibration lamp spectrum could be validated within 2% (see next section on the calibration lamp spectrum).

For case 2, the erroneous spectrum affects both the calibration and the actual measurement on the sample. Hence, a non-constant SF corrects for the average deviation of the measured spectrum from the true spectrum and improves the precision of the calculated iV_{oc}. The spectra of all optical components have been measured inhouse. Only the QE of the camera could not be validated. For the camera, only an approximated QE provided by the manufacturer (Figure S1) is available. Hence, the deviation in SF is most likely caused by an error in the QE of the camera. This implies that the error on the iV_{oc} is larger for wider bandgap filters, also described in Soufiani et al.[29] While the QE of the camera remains relatively flat as a plateau in the 650–850 nm range, it exhibits a steeper profile in the 950–1000 nm range. Consequently, even a slight shift in the QE can have a significant impact in the 950–1000 nm region on the iV_{oc} calculation, whereas it is negligible in the 650–850 nm region.
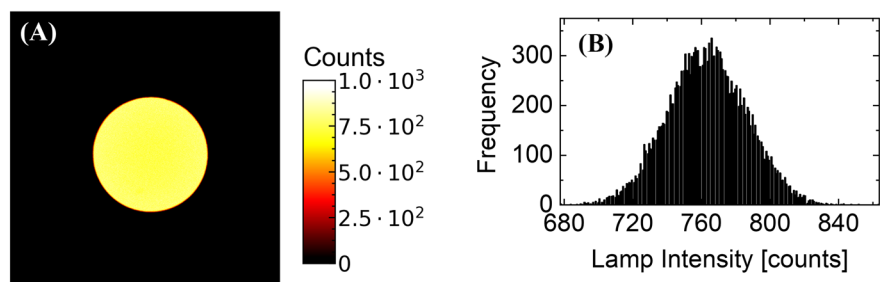
Effect of the calibration lamp

In this section, we investigate the uncertainties related to the calibration lamp used for our calibration procedure, where we determine SF from the arithmetic mean of the lamp image and the calibrated, and homogeneous photon flux $j_{ph,\ lamp}$ of the calibration lamp considering
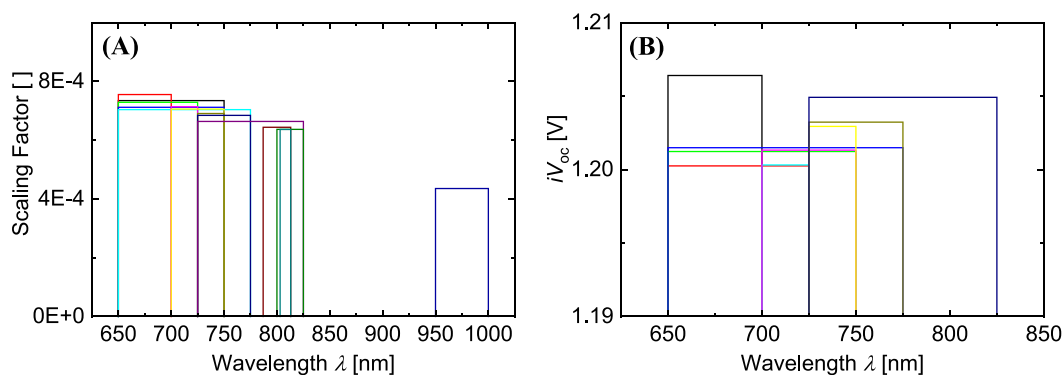
FIGURE 8 (A) Comparison of scaling factors SF for different bandpass filters. The vertical lines mark the opening and closing wavelength of the bandpass filters respectively. The horizontal lines mark the value of SF. (B) Comparison of mean iV_{oc} for the top cell of the III-V tandem solar cell presented in Figure 6 for different bandpass filters. For all filter combinations between 650 nm and 825 nm, the deviation is below 0.5% or 6 mV. Note that the largest deviations from the mean value of all filter combinations occur for the bandpass filters 650 nm to 700 nm (where the PL signal is very weak) and the bandpass filter 725 nm to 825 nm (where the absorptance or the top cell is very weak and measurement errors [noise] in the EQE used for the estimation of the absorptance become large).

FIGURE 9 (A) Measurement of the of the calibration lamp opening using a BP803-813 filter. (B) The histogram of the light intensity of the lamp in the region of interest.

the spectral response of the system according to Equation (1). Two potential sources of error can influence the results. The first source arises from the assumption of a homogeneous photon flux and pixel sensitivity (even though a flatfield calibration is routinely applied) all over the lamp opening. To assess the error associated with this assumption, we conducted an experiment using a neutral density ND1.8 filter placed in front of the camera. The acquisition was conducted for 0.5 s using a bandpass filter (BP803–813 nm). Figure 9A depicts the captured lamp image, and Figure 9B presents the histogram of the lamp intensity within the region of interest. The measured lamp signal yielded a mean value of 763.5 counts with a standard deviation of 22.9 counts. This standard deviation corresponds to an approximate 1–2 mV uncertainty in our iV_{oc} calculation.

The second source of error stems from variations in $j_{ph,lamp}$. To evaluate this, we employed a spectrophotometer to measure the relative lamp spectrum, which exhibited a similar shape to the datasheet provided by the supplier (see Figure 10) with deviations of below 2%. However, due to uncertainties in the calibration process, the lamp intensity has an uncertainty of 3% to 5% (depending on the spectral range) according to the manufacturer, resulting in an approximate error in the iV_{oc} of below 2 mV. Moreover, with prolonged usage, the lamp intensity may undergo a change, increasing the measurement uncertainty. The uncertainty in the total photon flux was checked using the WPVS cell presented in Figure 6. The solar cell was placed close to the calibration lamp and the short circuit current was determined. A current of 105.0 µA was expected according to the calibration data of the lamp and the EQE of the solar cell. In the experiment 99.2 µA were measured. This is a relative deviation of below 6%, leading to a variation of below 2 mV in the iV_{oc} calculation. Combining both sources of errors, the lamp introduces an uncertainty of approximately 4 mV in the iV_{oc} calculation in the worst-case scenario if calibration uncertainty and aging effect lead to a decreased actual photon flux.

Effect of the approximation of the absorptance

As described in the methods section, the determination of absorptance $A(E)$ in tandem solar cell samples can be approximated using either EQEs correctly scaled with spectrometric measurements or EQEs scaled to the $1-R$ spectrum, which corresponds to the total absorptance spectrum if no transmission is present. However, neither of these EQEs fully represent the actual absorptance of the system. The total absorptance of the tandem cell can be considered as an upper limit due to parasitic absorptance effects, while the EQE scaled
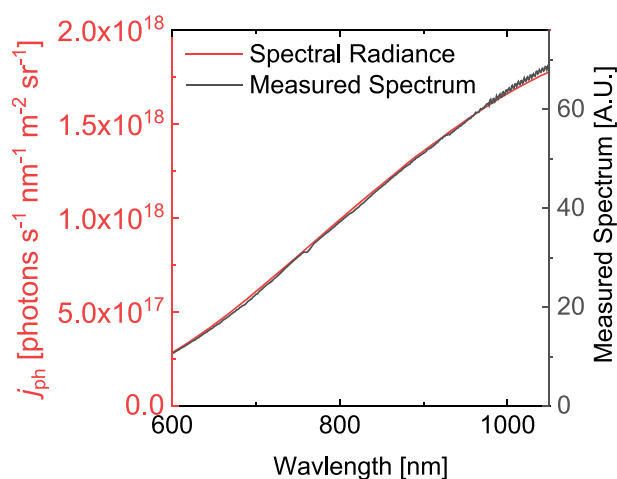

FIGURE 10 Spectrum of calibration lamp as provided from the manufacturer (red) and measured (black, in arbitrary units).

with spectrometric measurements represents a lower limit as the internal quantum efficiency of solar cells is less than unity.

As stated previously, it is suggested in literature that the deviation between $A(E)$ and $EQE(E)$ is very small or even negligible.[25] For samples that absolute EQEs cannot be measured for, relative EQEs must be scaled as described in Section 2. This approach adds an additional error. Generally, it holds true that $1 = R(E) + A_{para}(E) + A_{absorber}(E) + T(E)$. With the parasitic absorptance $A_{para}(E)$ and the absorptance in the photoactive absorber layer $A_{absorber}(E)$ adding up to the total absorptance. While close to the bandgap $T(E) > 0$, towards higher energies $T(E) = 0$ can be assumed without further restrictions for a solar cell that is not designed for semitransparent applications. However, depending on the applied charge transport layers and electrodes, $A_{para}(E_0) > 0$ for E_0 being the energy for which it holds true $1 - R(E_0) - EQE_{rel}(E_0) SF_{EQE} = 0$. Consequently, the assumption $EQE_{rel}(E_0) SF_{EQE} = 1 - R(E_0) = A_{para}(E) + A_{absorber}(E_0) \approx A_{absorber}(E_0)$ introduces an error in SF_{EQE}. This error depends on the solar cell structure but is in the range of few percent for recent perovskite silicon tandem solar cells. For example, for the device structure of the tandem solar cell in Figure 11 the error is below 3% according to simulations for both subcells.[21] This leads to an error smaller than 1 mV. The difference between absolute EQE and total absorptance for both perovskite top cells and silicon bottom cells in recent studies[47–50] on tandem devices is less than 5% (conservative

FIGURE 11 (A and B) iV_{oc} images of perovskite top cell and silicon bottom cell of a tandem device and (C) comparison between the total iV_{oc} of top and bottom cell and the terminal V_{oc}.
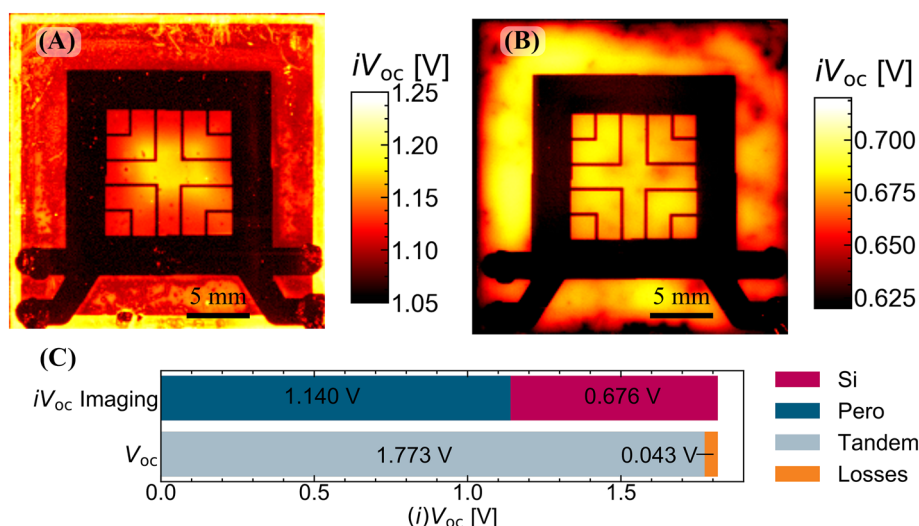
approximation from available plots in the corresponding publications), resulting in a total uncertainty of approximately 2 mV in the iV_{oc} calculation.

Effect of homogeneous illumination

Two lasers are used to illuminate the subcells under 1-sun equivalent conditions. For this, the required photon flux of the two lasers must be determined in the first step. For this, we use the method according to Meusel et al.[34] In this step, an error in the shape of the EQEs will translate into an erroneous target photon flux. The significance of this error depends on the precision of the EQE measurement setup and shall not be discussed here in further detail. However, most likely it is in the range of very few percent. In the second step, the laser must illuminate the whole region of interest homogeneously with the targeted illumination intensity. This introduces usually the more significant error compared to the first step. In our setup, the illumination intensity shows a variation of less than 3% on an area of 11×11 cm^2 for the 450 nm laser as well as the 808 nm. This deviation was determined by measuring the short-circuit current of the 2×2 cm^2 large WPVS silicon solar cell at 25 different equally distanced positions. Very small scaled inhomogeneities in the illumination intensity (speckling) cannot be resolved with this measurement. However, these inhomogeneities either cancel out through lateral charge carrier diffusion or are so small that they cannot be seen in the PL images. Hence this effect can also be neglected. In summary, the effect of the illumination intensity on the iV_{oc} images is expected to be in the range of 1 mV.

3.2 | Application to tandem solar cells

3.2.1 | Global voltage loss analysis

In this section, we employ our method to quantify the voltage loss in a two-terminal perovskite silicon tandem solar cell. The device

structure consists of p-type silicon hetero-junction bottom solar cell with a planar front side and a textured rear side and a p-i-n perovskite top solar. The top solar cell has the structure ITO/2PACz/Perovskite/C_{60}/SnO$_x$/ITO/Ag/MgF$_2$. The bandgap of the top cell is about 1.64 eV (756 nm). For more detailed information about the perovskite composition, please refer to our previous work by Heydarian et al.[21]

Figure 11A,B illustrates the iV_{oc} images of the perovskite top cell and silicon bottom cell, respectively, under 1-sun equivalent conditions. The arithmetic mean iV_{oc} values for the active area excluding fingers for the top cell and bottom cell are measured to be 1,140 mV and 676 mV, respectively. Additionally, Figure 11C presents a comparison of the total iV_{oc} obtained from our measurements with the terminal V_{oc}. It can be observed that there is a loss of 43 mV, which can be attributed to non-ideal energy band alignments at the contacts. This indicates the potential for further optimization to enhance the overall cell performance.

By quantifying the voltage loss at the contacts and determining subcell-selectively iV_{oc}, our method provides valuable insights for improving the efficiency of perovskite silicon tandem solar cells. Future optimization efforts can focus on bandgap alignments to minimize voltage losses and enhance the overall performance of the tandem device.

3.2.2 | Local voltage loss analysis

While the global assessment of the iV_{oc} is possible with our iV_{oc} imaging method using mean values, one of the key benefits of iV_{oc} imaging is the spatial resolution. In this section, this benefit is demonstrated on a monolithic perovskite silicon tandem solar cell. The analyzed tandem solar cell is composed of a textured p-type silicon hetero-junction bottom solar cell and a p-i-n perovskite top solar cell. A FA$_{0.85}$Cs$_{0.15}$Pb(I$_{0.78}$Br$_{0.22}$)$_3$ perovskite absorber is deposited for the top cell using the hybrid route. 2PACZ and C_{60}/Sno$_x$ are used as hole
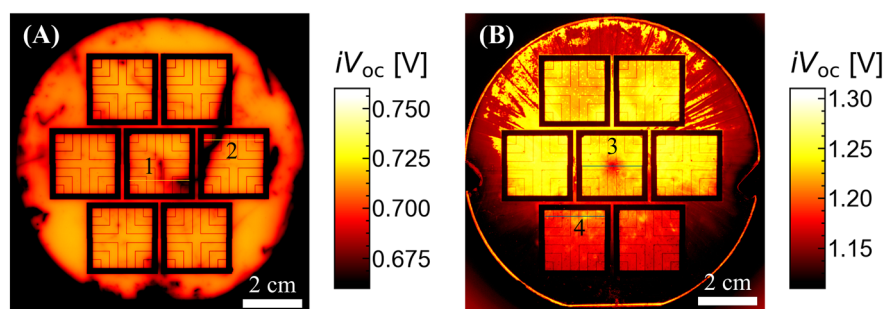
FIGURE 12 iV_{oc} image of (A) the silicon bottom cells and (B) the perovskite top cells of tandem devices, revealing local losses. The lines labelled 1–4 are cross sections further analyzed in Figure 13.
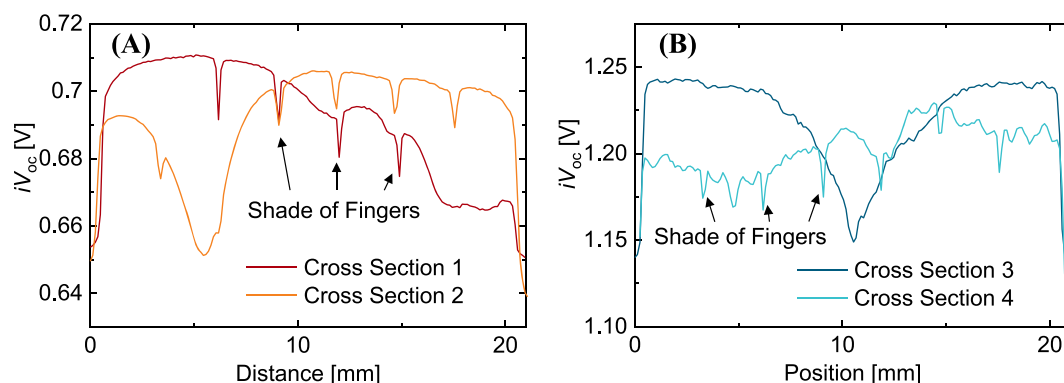
FIGURE 13 Cross sections of the iV_{oc} images in Figure 12 of (A) the silicon and (B) the perovskite subcell of the perovskite silicon tandem solar cell. The position of the cross sections is marked in Figure 12.

and electron transport layers respectively. The bandgap is approximately 1.66 eV (747 nm).

Figure 12 displays the iV_{oc} images of seven silicon bottom cells and perovskite top cells on one substrate. Additionally, Figure 13 shows the spatially resolved iV_{oc} of two cross sections of the silicon iV_{oc} image in Figure 12A and two cross sections of the perovskite iV_{oc} image in Figure 12B. While most parts of the presented tandem solar cells are well performing and homogeneous, the chosen cross sections cover local inhomogeneities. A natural inhomogeneity is the presence of fingers and busbars, shading the PL signal from the solar cell and hindering the local iV_{oc} determination. While this cannot be circumvented, other defects of the cell can be prevented by changes in the manufacturing routine. As Figure 13A depicts, a line shaped defect in the silicon bottom cell leads to a local decrease in iV_{oc} by approximately 50 mV compared to other well performing parts of the cells for both cross sections. Several inhomogeneities are visible in the perovskite sub cell in Figure 13B. Cross section 3 features a very local defect decreasing iV_{oc} by approximately 93 mV. Cross section 4 features a larger patterned inhomogeneity resulting in a loss of approximately 50 mV across a larger region compared to the well performing parts of cross section 4.

All these local features are not detectable in global V_{oc} or iV_{oc} measurements. In consequence, it is hard to attribute low V_{oc} to its

root cause without iV_{oc} imaging. Similarly, the result of spatially non-resolved iV_{oc} highly depends on the region that is probed on inhomogeneous samples. This hinders the comparison of different batches and can lead to wrong conclusions in the worst case.

4 | CONCLUSION AND OUTLOOK

In summary, we have demonstrated a new iV_{oc} imaging method to generate spatially resolved iV_{oc} images of various types of single junction and tandem solar cells based on the PL imaging technique. This iV_{oc} imaging method offers the advantages of being rapid, contactless, and subcell-selective, making it suitable for large-area multijunction solar cells. Since the method uses camera-based imaging and not point-by-point mapping, the quality of devices can effectively be monitored at high resolution with short measurement times. The largest samples presented in this report, for example, show a resolution on the 100 μm-scale even for cell sizes of around $11 \times 11 \, cm^2$. However, solar cells with the industrial wafer format M12 could be measured with no major changes to the measurement setup as well. The method allows to pinpoint the causes of device failure and accelerate process and material optimization. In contrast to traditional V_{oc} measurements, our iV_{oc} imaging method can be applied to uncompleted

devices without electrical contacts. Furthermore, our method allows for the evaluation of individual layers, making it particularly valuable during early-stage sample preparation and characterization for tandem devices. The measurement error is experimentally found to be very small. The deviation is no larger than 0.8% for any of the applied validation methods. The overall estimated impact of errors of the band-pass filters, the calibration lamp, the determination of the absorbance spectrum and the sample illumination on the calculated iV_{oc} is in the range of well below 10 mV.

The presented method was developed to characterize perovskite silicon tandem solar cells. However, it is not limited to this solar cell technology. It can be applied to various types of solar cells, if suitable excitation light sources and band pass filters are available to properly detect the PL signal subcell-selectively. Therefore, it also allows its application to, for example, silicon perovskite perovskite triple junction solar cells. It remains part of a future work to apply this method under electrical bias conditions to analyze charge carrier extraction properties. Without any limitations, the method can also be used to convert electroluminescence images into iV_{oc} images.

AUTHOR CONTRIBUTIONS

Anh Dinh Bui and Oliver Fischer contributed in equal parts to this publication. They developed the measurement method, planned, and evaluated the PL measurements and wrote the manuscript. Oliver Fischer conducted the spectrally integrated PL measurements. Anh Dinh Bui wrote the first version of the evaluation script and performed the PL measurements on the hyperspectral measurement setup. Florian Schindler, Stefan W. Glunz, Daniel Macdonald, Martin C. Schubert, and Hieu T. Nguyen supervised the work. All authors reviewed the manuscript.

ACKNOWLEDGEMENTS

CONFLICT OF INTEREST STATEMENT

The authors declare no conflict of interest.

DATA AVAILABILITY STATEMENT

The data that support the findings of this study are available from the corresponding author upon reasonable request.

ORCID

Oliver Fischer https://orcid.org/0009-0006-9544-4246
Anh Dinh Bui https://orcid.org/0000-0002-9660-6132
Florian Schindler https://orcid.org/0000-0001-7639-2758
Stefan W. Glunz https://orcid.org/0000-0002-9877-2097

REFERENCES

1. National Renewable Energy Laboratory. Best research-cell efficiency chart. 2023. Accessed 31 July 2023. https://www.nrel.gov/pv/cell-efficiency.html
2. de Vos A. Detailed balance limit of the efficiency of tandem solar cells. *J Phys D Appl Phys*. 1980;13(5):839-846. doi:10.1088/0022-3727/13/5/018
3. Brown AS, Green MA. Detailed balance limit for the series constrained two terminal tandem solar cell. *Physica E*. 2002;14(1-2):96-100. doi:10.1016/S1386-9477(02)00364-8
4. Futscher MH, Ehrler B. Efficiency limit of perovskite/Si tandem solar cells. *ACS Energy Lett*. 2016;1(4):863-868. doi:10.1021/acsenergylett.6b00405
5. Green MA, Dunlop ED, Yoshita M, et al. Solar cell efficiency tables (version 62). *Prog Photovoltaics*. 2023;31(7):651-663. doi:10.1002/pip.3726
6. He J, Sheng W, Yang J, et al. Omnidirectional diffusion of organic amine salts assisted by ordered arrays in porous lead iodide for two-step deposited large-area perovskite solar cells. *Energ Environ Sci*. 2023;16(2):629-640. doi:10.1039/D2EE03418B
7. Luo X, Luo H, Li H, et al. Efficient perovskite/silicon tandem solar cells on industrially compatible textured silicon. *Adv Mater Weinheim*. 2023;35(9):e2207883. doi:10.1002/adma.202207883
8. Macpherson S, Doherty TAS, Winchester AJ, et al. Local nanoscale phase impurities are degradation sites in halide perovskites. *Nature*. 2022;607(7918):294-300. doi:10.1038/s41586-022-04872-1
9. Jošt M, Kegelmann L, Korte L, Albrecht S. Monolithic perovskite tandem solar cells: a review of the present status and advanced characterization methods toward 30% efficiency. *Adv Energy Mater*. 2020;10(26):1904102. doi:10.1002/aenm.201904102
10. Sinton RA, Cuevas A. Contactless determination of current–voltage characteristics and minority-carrier lifetimes in semiconductors from quasi-steady-state photoconductance data. *Appl Phys Lett*. 1996;69(17):2510-2512. doi:10.1063/1.117723
11. Tress W, Yavari M, Domanski K, et al. Interpretation and evolution of open-circuit voltage, recombination, ideality factor and subgap defect states during reversible light-soaking and irreversible degradation of perovskite solar cells. *Energ Environ Sci*. 2018;11(1):151-165. doi:10.1039/C7EE02415K
12. Bui AD, Mozaffari N, Truong TN, et al. Electrical properties of perovskite solar cells by illumination intensity and temperature-dependent photoluminescence imaging. *Prog Photovoltaics*. 2021;30(8):1038-1044. doi:10.1002/pip.3498

13. Rietwyk KJ, Lin X, Tan B, et al. Ideality factor mapping of back-contact perovskite solar cells. *Adv Energy Mater*. 2023;13(9):2200796. doi:10.1002/aenm.202200796

14. Stolterfoht M, Caprioglio P, Wolff CM, et al. The impact of energy alignment and interfacial recombination on the internal and external open-circuit voltage of perovskite solar cells. *Energ Environ Sci*. 2019;12(9):2778-2788. doi:10.1039/C9EE02020A

15. Stolterfoht M, Grischek M, Caprioglio P, et al. How to quantify the efficiency potential of neat perovskite films: perovskite semiconductors with an implied efficiency exceeding 28. *Adv Mater Weinheim*. 2020;32(17):e2000080. doi:10.1002/adma.202000080

16. Fischer O, Fell A, Messmer C, et al. Understanding contact nonuniformities at interfaces in perovskite silicon tandem solar cells using luminescence imaging, lock-in thermography, and 2D/3D simulations. *Sol RRL*. 2023;7(19):2300249. doi:10.1002/solr.202300249

17. Caprioglio P, Stolterfoht M, Wolff CM, et al. On the relation between the open-circuit voltage and quasi-Fermi level splitting in efficient perovskite solar cells. *Adv Energy Mater*. 2019;9(33):1901631. doi:10.1002/aenm.201901631

18. Chen S, Zhu L, Yoshita M, et al. Thorough subcells diagnosis in a multi-junction solar cell via absolute electroluminescence-efficiency measurements. *Sci Rep*. 2015;5(1):7836. doi:10.1038/srep07836

19. Alonso-Alvarez D, Ekins-Daukes N. Photoluminescence-based current–voltage characterization of individual subcells in multijunction devices. *IEEE J Photovolt*. 2016;6:1004-1011. doi:10.1109/JPHOTOV.2016.2547583

20. Al-Ashouri A, Marčinskas M, Kasparavičius E, et al. Wettability improvement of a carbazole-based hole-selective monolayer for reproducible perovskite solar cells. *ACS Energy Lett*. 2023;8(2):898-900. doi:10.1021/acsenergylett.2c02629

21. Heydarian M, Messmer C, Bett AJ, et al. Maximizing current density in monolithic perovskite silicon tandem solar cells. *Sol RRL*. 2023;7(7). doi:10.1002/solr.202200930

22. Heinz FD, Mundt LE, Warta W, Schubert MC. A combined transient and steady state approach for robust lifetime spectroscopy with micrometer resolution. *Phys Status Solidi RRL*. 2015;9(12):697-700. doi:10.1002/pssr.201510364

23. Tebyetekerwa M, Zhang J, Liang K, et al. Quantifying quasi-Fermi level splitting and mapping its heterogeneity in atomically thin transition metal dichalcogenides. *Adv Mater Weinheim*. 2019;31(25):e1900522. doi:10.1002/adma.201900522

24. Delamarre A, Lombez L, Guillemoles J-F. Contactless mapping of saturation currents of solar cells by photoluminescence. *Appl Phys Lett*. 2012;100(13):131108. doi:10.1063/1.3697704

25. El-Hajje G, Momblona C, Gil-Escrig L, et al. Quantification of spatial inhomogeneity in perovskite solar cells by hyperspectral luminescence imaging. *Energ Environ Sci*. 2016;9(7):2286-2294. doi:10.1039/C6EE00462H

26. Giesecke JA, Schubert MC, Walter D, Warta W. Minority carrier lifetime in silicon wafers from quasi-steady-state photoluminescence. *Appl Phys Lett*. 2010;97(9):92109. doi:10.1063/1.3485216

27. Giesecke JA, Schubert MC, Michl B, Schindler F, Warta W. Minority carrier lifetime imaging of silicon wafers calibrated by quasi-steady-state photoluminescence. *Photovolt Solar Energy Mater Technol*. 2011;95(3):1011-1018. doi:10.1016/j.solmat.2010.12.016

28. Giesecke JA, Michl B, Schindler F, Schubert MC, Warta W. Minority carrier lifetime of silicon solar cells from quasi-steady-state photoluminescence. *Photovolt Solar Energy Mater Technol*. 2011;95(7):1979-1982. doi:10.1016/j.solmat.2011.02.023

29. Soufiani AM, Lee-Chin R, Fassl P, et al. Implied open-circuit voltage imaging via a single bandpass filter method—its first application in perovskite solar cells. *Adv Funct Mater*. 2022;2210592. doi:10.1002/adfm.202210592

30. Bui AD, Mahmud MA, Mozaffari N, et al. Contactless and spatially resolved determination of current−voltage curves in perovskite solar cells via photoluminescence. *Sol RRL*. 2021;5(8):2100348. doi:10.1002/solr.202100348

31. Trupke T, Bardos RA, Abbott MD, Cotter JE. Suns-photoluminescence: contactless determination of current-voltage characteristics of silicon wafers. *Appl Phys Lett*. 2005;87(9):093503. doi:10.1063/1.2034109

32. Michl B, Impera D, Bivour M, Warta W, Schubert MC. Suns-PLI as a powerful tool for spatially resolved fill factor analysis of solar cells. *Prog Photovoltaics*. 2012;22(5):581-586. doi:10.1002/pip.2293

33. Lang F, Köhnen E, Warby J, et al. Revealing fundamental efficiency limits of monolithic perovskite/silicon tandem photovoltaics through subcell characterization. *ACS Energy Lett*. 2021;6(11):3982-3991. doi:10.1021/acsenergylett.1c01783

34. Meusel M, Adelhelm R, Dimroth F, Bett AW, Warta W. Spectral mismatch correction and spectrometric characterization of monolithic III-V multi-junction solar cells. *Prog Photovoltaics*. 2002;10(4):243-255. doi:10.1002/pip.407

35. Ory D, Paul N, Lombez L. Extended quantitative characterization of solar cell from calibrated voltage-dependent electroluminescence imaging. *J Appl Phys*. 2021;129(4):43106. doi:10.1063/5.0021095

36. Wurfel P. The chemical potential of radiation. *J Phys C: Solid State Phys*. 1982;15(18):3967-3985. doi:10.1088/0022-3719/15/18/012

37. Würfel P, Finkbeiner S, Daub E. Generalized Planck's radiation law for luminescence via indirect transitions. *Appl Phys A*. 1995;60(1):67-70. doi:10.1007/BF01577615

38. Messmer C, Goraya BS, Nold S, et al. The race for the best silicon bottom cell: efficiency and cost evaluation of perovskite–silicon tandem solar cells. *Prog Photovoltaics*. 2021;29(7):744-759. doi:10.1002/pip.3372

39. Trupke T. Absorptivity of silicon solar cells obtained from luminescence. *Sol Energy Mater Sol Cells*. 1998;53(1-2):103-114. doi:10.1016/S0927-0248(98)00016-6

40. Hameiri Z, Mahboubi Soufiani A, Juhl MK, et al. Photoluminescence and electroluminescence imaging of perovskite solar cells. *Prog Photovolt: Res Appl*. 2015;23(12):1697-1705. doi:10.1002/pip.2716

41. Meusel M, Baur C, Létay G, Bett AW, Warta W, Fernandez E. Spectral response measurements of monolithic GaInP/Ga (In)As/Ge triple-junction solar cells: measurement artifacts and their explanation. *Prog Photovolt: Res Appl*. 2003;11(8):499-514. doi:10.1002/pip.514

42. Mundus M, Venkataramanachar B, Gehlhaar R, et al. Spectrally resolved nonlinearity and temperature dependence of perovskite solar cells. *Sol Energy Mater Sol Cells*. 2017;172:66-73. doi:10.1016/j.solmat.2017.07.013

43. Saliba M, Etgar L. Current density mismatch in perovskite solar cells. *ACS Energy Lett*. 2020;5(9):2886-2888. doi:10.1021/acsenergylett.0c01642

44. Bett AJ, Chojniak D, Schachtner M, et al. Spectrometric characterization of monolithic perovskite/silicon tandem solar cells. *Sol RRL*. 2023;7(2):2200948. doi:10.1002/solr.202200948

45. Dimroth F, Beckert R, Meusel M, Schubert U, Bett AW. Metamorphic $Ga_yIn_{1-y}P/Ga_{1-x}In_xAs$ tandem solar cells for space and for terrestrial concentrator applications at C > 1000 suns. *Prog Photovoltaics*. 2001;9(3):165-178. doi:10.1002/pip.362

46. Rakocevic L, Mundt LE, Gehlhaar R, et al. Loss analysis in perovskite photovoltaic modules. *Sol RRL*. 2019;3(12):1900338. doi:10.1002/solr.201900338

47. Sahli F, Werner J, Kamino BA, et al. Fully textured monolithic perovskite/silicon tandem solar cells with 25.2% power conversion efficiency. *Nat Mater*. 2018;17(9):820-826. doi:10.1038/s41563-018-0115-4

48. Köhnen E, Wagner P, Lang F, et al. 27.9% efficient monolithic perovskite/silicon tandem solar cells on industry compatible bottom cells. *Sol RRL*. 2021;5(7):2100244. doi:10.1002/solr.202100244

49. Tockhorn P, Sutter J, Cruz A, et al. Nano-optical designs for high-efficiency monolithic perovskite-silicon tandem solar cells. *Nat Nanotechnol*. 2022;17(11):1214-1221. doi:10.1038/s41565-022-01228-8

50. Mariotti S, Köhnen E, Scheler F, et al. Interface engineering for high-performance, triple-halide perovskite–silicon tandem solar cells. *Science*. 2023;381(6653):63-69. doi:10.1126/science.adf5872

SUPPORTING INFORMATION

Additional supporting information can be found online in the Supporting Information section at the end of this article.